

# Homodyne Measurement of a Non-Hermitian Qubit Undergoing Fluorescence

Roson Nongthombam<sup>1,\*</sup> and Amarendra K. Sarma<sup>1,†</sup>

<sup>1</sup>*Department of Physics, Indian Institute of Technology Guwahati, Guwahati-781039, (India)*

(Dated: October 27, 2025)

Implementation of a two-level non-Hermitian qubit via postselection of a three-level system has been demonstrated. The post-selection procedure, which discards quantum jump to the ground-state manifold  $|g\rangle$  while retaining excitations in the  $|e\rangle$  and  $|f\rangle$  manifolds, effectively generates a non-Hermitian qubit exhibiting  $\mathcal{PT}$  symmetry. In this work, we perform continuous homodyne measurement of this non-Hermitian qubit and analyze the interplay between decay introduced by post-selection and measurement backaction. We compare the ensemble-averaged dynamics obtained from measurement trajectories with the Liouvillian average. We formulate the no-jump stochastic differential equation describing the postselected non-Hermitian qubit and show that its ensemble-averaged dynamics agree with those of the jump-updated postselected evolution at drive strengths far from the Liouvillian exceptional point (EP). The degree of deviation near the EP depends sensitively on the nature of the drive. This discrepancy is attributed to the interplay between measurement backaction and the non-Hermitian decay introduced by post-selection. Furthermore, we determine the optimal path of the non-Hermitian qubit by extremizing the action within the path-integral formulation of the quantum trajectory framework. Our results provide insights into how measurement backaction and non-Hermitian dynamics together shape the transient behavior of open quantum systems and enable controlled manipulation of qubits near exceptional points.

## I. INTRODUCTION

Unlike a Hermitian quantum system, where the evolution is coherent, unitary, and trace-preserving, the evolution of a non-Hermitian system is still coherent but non-unitary and non-trace-preserving. Such systems inherently include loss and gain channels, and when driven, they can exhibit parity-time ( $\mathcal{PT}$ ) symmetry breaking transitions, where the energy spectrum changes from being purely real to imaginary [1–3]. The transition point is known as the exceptional point (EP) of the non-Hermitian system. A non-Hermitian system with only loss or only gain channels can also exhibit an EP. At the EP, the eigenvalues coalesce and the corresponding eigenvectors become parallel (i.e., linearly dependent) [4–6]. Non-Hermitian systems have been realized in various classical platforms [7–12], and transitions in the vicinity of EPs have been exploited in a range of applications [13–19].

In a generic two-level system, non Hermiticity and the EP can be introduced either by making one of the levels lossy or amplifying (gain), or by assigning loss to one level and gain to the other, while keeping the two-levels coherently coupled. In the latter case, the system exhibits  $\mathcal{PT}$  symmetry. In both scenarios, when the coupling strength between the two-levels becomes comparable to the loss or gain, the system reaches an EP. For the  $\mathcal{PT}$  symmetric case, where one level experiences gain and the other loss, the system supports coherent oscillations of population between the two-levels in the unbroken  $\mathcal{PT}$  symmetric phase. In contrast, in the broken  $\mathcal{PT}$  symmetric phase,

the population either grows or decays exponentially without oscillations [20]. If spontaneous emission or quantum jumps of population between the levels are included, the degeneracy of eigenvalues at the EP is lifted, and the system exhibits a second order exceptional point [10, 21]. In the unbroken  $\mathcal{PT}$  symmetric phase, the dynamics show decaying oscillations, whereas in the broken  $\mathcal{PT}$  symmetric phase, the system becomes overdamped. The inclusion of quantum jumps implies that the presence of an EP can only be observed in the transient dynamics of the system [22]. This is because the eigenstates corresponding to the EP are unphysical in the steady state: the system always decays into the eigenstate associated with the smallest decay rate, which does not correspond to the EP [10, 21].

Here we consider a two-level non-Hermitian system constructed via post-selection on a three-level system, following the approach studied in a superconducting qubit platform [20, 23, 24]. The post-selection is carried out by discarding all measurement outcomes in which the system goes to the ground state manifold  $|g\rangle$ , and retaining only those in which the population remains in the first excited state  $|e\rangle$  or the second excited state  $|f\rangle$  manifold [20]. This effectively reduces the three-level system to a non Hermitian two-level system, or a non Hermitian qubit. This system exhibits  $\mathcal{PT}$  symmetry, where the dynamics are governed by the difference between the eigenvalues. In the presence of quantum jumps between  $|e\rangle$  and  $|f\rangle$  states, all of the results discussed previously for  $\mathcal{PT}$  symmetric systems apply here as well. In this work, we study the homodyne measurement of the non-Hermitian qubit undergoing spontaneous emission. Continuous homodyne measurement of a simple two-level system undergoing spontaneous emission has been studied in [25–31]. Here, we apply the same measurement approach to the non-Hermitian qubit obtained via post-

\* [n.roson@iitg.ac.in](mailto:n.roson@iitg.ac.in)

† [aksarma@iitg.ac.in](mailto:aksarma@iitg.ac.in)

selection. In this approach, photons emitted from the qubit are continuously collected and monitored, and the qubit state is inferred from the stochastic trajectories generated by the measurement record. The theoretical foundation for this description lies in quantum measurement theory within the quantum trajectory framework, which is a well-studied field [30, 32–46]. By performing the measurement, we study the interplay between the non-Hermitian decay introduced by post-selection and the measurement backaction arising from homodyne detection. The ensemble-averaged dynamics obtained from measurement trajectories agree with the Liouvillian average. We then derive the no-jump stochastic differential equation describing the postselected non-Hermitian qubit and compare its dynamics with the Liouvillian evolution. The ensemble-averaged dynamics from this no-jump equation agree with the Liouvillian only at drive strengths far from the exceptional point (EP). Near the EP, the deviation is dependent on the axis of the drive. This dependence is evident in whether the system is driven about the  $x$ -axis or the  $y$ -axis of the qubit's Bloch vector. We further show the optimal path of the measurement process by incorporating the path integral formalism in the quantum trajectory framework [47–51].

The paper is organized as follows. In Section II, we discuss different measurement setups that unravel quantum trajectories. We define the Kraus operators associated with these setups and analyze the resulting trajectories. Section III focuses on the post-selection of trajectories and the definition of the non-Hermitian qubit. In Section IV, we compare the dynamics of the qubit obtained through two approaches: one based on the Liouvillian restricted to the qubit manifold, and the other derived from averaging the postselected trajectories. In Section V, we derive the stochastic master equation for the non-Hermitian qubit under homodyne detection and study the combined effects of measurement backaction and post-selection. Section VI presents the optimal paths of the qubit using a path-integral formalism. Finally, in Section VII, we provide a brief summary of the work.

## II. HYBRID MEASUREMENT SETUP OF THE THREE-LEVEL SYSTEM

Let us consider the measurement of a generic three-level system which interacts with an environment or a cavity. Assuming no interaction between the system and the environment initially, the state of the system plus environment is given as

$$|\Psi(0)\rangle = (c_g |g\rangle + c_e |e\rangle + c_f |f\rangle) \otimes |E\rangle, \quad (1)$$

where  $|f\rangle$ ,  $|e\rangle$ , and  $|g\rangle$  are the second excited state, first excited state, and ground state, respectively.  $|E\rangle$  is the state of the environment. The quantities  $|c_g|^2$ ,  $|c_e|^2$ , and  $|c_f|^2$  represent the probabilities of finding the system in the states  $|g\rangle$ ,  $|e\rangle$ , and  $|f\rangle$ , respectively. The system interacts with the environment and undergoes spontaneous

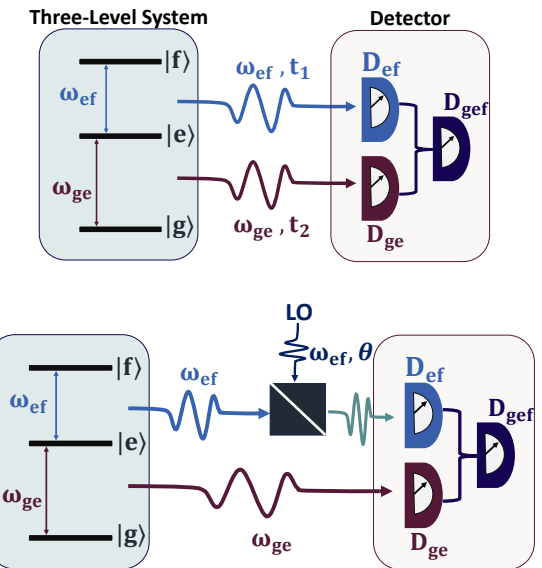


FIG. 1. Measurement schemes of the three-level system illustrating different unraveling models of its trajectories. The system emits photons that are directed to the detector via the environment or a cavity. The detector has three components. One part ( $D_{ef}$ ) detects photons released from the  $|f\rangle \rightarrow |e\rangle$  transition with frequency  $\omega_{ef}$ , and another ( $D_{eg}$ ) detects photons from the  $|e\rangle \rightarrow |g\rangle$  transition with frequency  $\omega_{ge}$ . The detected signals from these two components are sent to  $D_{gef}$ , where the final state update happens. The schematic shows two types of measurement. The top figure shows pure photon-counting detection: at some time  $t_1$ , when a jump from  $|f\rangle$  to  $|e\rangle$  occurs,  $D_{ef}$  clicks; at some other time  $t_2$ , when a jump from  $|e\rangle$  to  $|g\rangle$  occurs,  $D_{eg}$  clicks. In the former case, the detector  $D_{gef}$  updates the state according to the Kraus operator  $K_{1e}$ , and in the latter according to  $K_{1g}$ . When no jump occurs, the state is always updated according to  $K_0$ . The bottom figure shows a hybrid measurement scheme: the jump from  $|f\rangle$  to  $|e\rangle$  is continuously and weakly monitored through a homodyne measurement setup, while the jump from  $|e\rangle$  to  $|g\rangle$  is monitored by photon counting measurement. The weak and continuous homodyne measurement is realized by inserting a beam splitter in front of the detector, and a local oscillator of frequency  $\omega_{ef}$  and phase  $\theta$  (with respect to the  $|f\rangle \rightarrow |e\rangle$  photon) is sent to the beam splitter. We assume that, because of the frequency mismatch, the  $|e\rangle \rightarrow |g\rangle$  photon is sent to the photon-counting channel. As long as there is no jump from  $|e\rangle$  to  $|g\rangle$ , the detector  $D_{gef}$  updates the state as per  $K_H$ , and upon detection it updates via  $K_J$ .

emission from  $|f\rangle$  to  $|e\rangle$  or from  $|e\rangle$  to  $|g\rangle$ , all of which have different transition frequencies. There is no direct transition from  $|f\rangle$  to  $|g\rangle$ . The system plus environment state then evolves according to  $|\Psi(t)\rangle = U_e |\Psi(0)\rangle$ , where  $U_e$  is the unitary operator describing the interaction between the system and the environment. Instead of defining the exact form of  $U_e$  and finding the state at an arbitrary time  $t$ , we phenomenologically consider the evolved

state as

$$\begin{aligned} |\Psi(t+dt)\rangle &= c_e(t)\sqrt{p_g}|g\rangle|E_{1g}\rangle + c_f(t)\sqrt{p_e}|e\rangle|E_{1e}\rangle \\ &+ (c_g(t)|g\rangle + c_e(t)\sqrt{1-p_g}|e\rangle \\ &+ c_f(t)\sqrt{1-p_e}|f\rangle)|E_0\rangle, \end{aligned} \quad (2)$$

where  $|E_0\rangle$  is the state of the environment when no photon is emitted from the system, whereas  $|E_{1g}\rangle$  and  $|E_{1e}\rangle$  are the environment states when the system emits a photon from  $|e\rangle$  to  $|g\rangle$  with probability  $p_g = \gamma_g dt$  and from  $|f\rangle$  to  $|e\rangle$  with probability  $p_g = \gamma_e dt$ , respectively. Here,  $\gamma_e = 1/T_e$  and  $\gamma_g = 1/T_g$  are the characteristic rates at which the system undergoes spontaneous emission.

The environment captures the emitted photon from the system during the spontaneous emission and directs it to a detector as shown in Fig.1. As discussed in the figure, we assume that the detector is able to distinguish between the  $|f\rangle \rightarrow |e\rangle$  transition photon and the  $|e\rangle \rightarrow |g\rangle$  photon. We also assume that  $dt \ll T_e, T_g$  (i.e.,  $\gamma_e dt \ll 1$  and  $\gamma_g dt \ll 1$ ), so that the detector is Markovian. When no photon is emitted from the system at time  $t+dt$ , the detector measures the system's state by projecting onto the environment state  $|E_0\rangle$ , resulting in  $|\Psi(t+dt)\rangle_s = \langle E_0|\Psi(t+dt)\rangle = K_0|\Psi(t)\rangle_s$ , where  $K_0$  is the corresponding Kraus operator. In contrast, if a photon is emitted due to the transition  $|f\rangle \rightarrow |e\rangle$ , the detector projects onto the environment state  $|E_{1e}\rangle$ , giving  $\langle E_{1e}|\Psi(t+dt)\rangle = K_{1e}|\Psi(t)\rangle_s$ , with  $K_{1e}$  as the associated Kraus operator. Similarly, when the photon emission arises from the transition  $|e\rangle \rightarrow |g\rangle$ , the projection onto  $|E_{1g}\rangle$  yields  $\langle E_{1g}|\Psi(t+dt)\rangle = K_{1g}|\Psi(t)\rangle_s$ , where  $K_{1g}$  represents the corresponding Kraus operator for that process. The three Kraus operators can be obtained from the Kraus matrix

$$M = \begin{bmatrix} \sqrt{1-p_g} & 0 & 0 \\ \sqrt{p_g}\hat{a}_e^\dagger & \sqrt{1-p_g} & 0 \\ 0 & \sqrt{p_g}\hat{a}_g^\dagger & 1 \end{bmatrix}, \quad (3)$$

Here, the Kraus operators are defined as  $K_0 = \langle E_0|M|E_0\rangle$ ,  $K_{1g} = \langle E_{1g}|M|E_0\rangle$ , and  $K_{1e} = \langle E_{1e}|M|E_0\rangle$ , where the creation operators act on the environment state as  $\hat{a}_e^\dagger|E_0\rangle = |E_{1e}\rangle$  and  $\hat{a}_g^\dagger|E_0\rangle = |E_{1g}\rangle$ , and the environment states are assumed to be orthonormal. Note that this measurement scheme illustrates one of the unraveling models for the trajectories in a three-level measurement.

We now consider another trajectory unraveling model using a hybrid detection scheme, which continuously monitors the  $|f\rangle \rightarrow |e\rangle$  transition while simultaneously photon-counting the  $|e\rangle \rightarrow |g\rangle$  jump, as shown in Fig. 1. Since the system has different transition frequencies, we assume that the hybrid detector can distinguish between the emissions and is able to use different measurement setups for the different transitions as discussed in the figure. The hybrid detector continuously monitors the  $|f\rangle \rightarrow |e\rangle$  quantum jump via weak homodyne detection.

When a jump from  $|e\rangle$  to  $|g\rangle$  occurs, the population in  $|e\rangle$  and  $|f\rangle$  vanishes, the system collapses into  $|g\rangle$ . The state update of this detection process can be described using the Kraus operators of the detector  $D_{\text{gef}}$ . When no jump is registered, the operator is

$$K_H = \sqrt{N}e^{-r^2 dt/4} \begin{bmatrix} \sqrt{1-\gamma_e dt} & 0 & 0 \\ r dt \sqrt{\gamma_e} e^{-i\theta} & \sqrt{1-\gamma_g dt} & 0 \\ 0 & 0 & 1 \end{bmatrix}, \quad (4)$$

where  $r$  is the measurement signal from the homodyne detection and  $\theta$  is the phase difference between the  $|f\rangle \rightarrow |e\rangle$  transition and the local oscillator (refer Appendix A). When a jump is registered, the operator is

$$K_J = \sqrt{N}e^{-r^2 dt/4} \begin{bmatrix} 0 & 0 & 0 \\ 0 & 0 & 0 \\ 0 & \sqrt{\gamma_g dt} & 0 \end{bmatrix}. \quad (5)$$

The measurement Kraus operators  $K_H$  and  $K_J$  satisfy the POVM condition, i.e.,  $\int dr (K_H^\dagger K_H + K_J^\dagger K_J) = \mathbb{I}$ , which yields the normalization factor  $N = \sqrt{dt/2\pi}$ . The state update of the system, depending on whether a jump is registered or not, is given by

$$\rho(t+dt)|_{H,J} = \frac{U K_{H,J} \rho(t) K_{H,J}^\dagger U^\dagger}{\text{tr}(U K_{H,J} \rho(t) K_{H,J}^\dagger U^\dagger)}, \quad (6)$$

where  $U$  is the unitary evolution operator of the system and the subscript  $H$  or  $J$  corresponds to the homodyne or jump measurement, respectively.

A single measurement trajectory can be obtained by updating the state at every interval  $dt$  up to some total measurement time  $T$ . Each trajectory corresponds to a pure state. An example of such trajectories is shown in Fig.2. We consider the  $|f\rangle$  and  $|e\rangle$  states to be coherently driven such that  $U = \exp(-i\omega(|f\rangle\langle f| + |e\rangle\langle e|)dt)$ . As seen from the figure, when no jump from  $|e\rangle$  to  $|g\rangle$  occurs, the system stochastically oscillates between the  $|f\rangle$  and  $|e\rangle$  states, and as soon as a jump from  $|e\rangle$  to  $|g\rangle$  is registered, the trajectory collapses into the ground state and remains there until the end of the measurement time. By averaging over many such trajectories, an ensemble-averaged dynamics of the system can be obtained, which corresponds to a mixed state. To validate the hybrid detector protocol, we compare the average dynamics obtained from the trajectory ensemble with those obtained from the Lindblad master equation (see Appendix A). We plot the second excited state probability  $\rho_{ff}(t)$ , the first excited state probability  $\rho_{ee}(t)$ , and the ground state probability  $\rho_{gg}(t)$  of the average dynamics from both approaches in Fig.2(d), where the probabilities match excellently.

In the experiment Ref. [20, 21], the measurement of the  $|e\rangle$  and  $|f\rangle$  postselected manifold is realized by performing a homodyne measurement of the signal emitted from the three-level system using a Josephson parametric amplifier. The homodyne measurement detects the

system-state-dependent shift of the cavity frequency and thereby determines the state of the system.

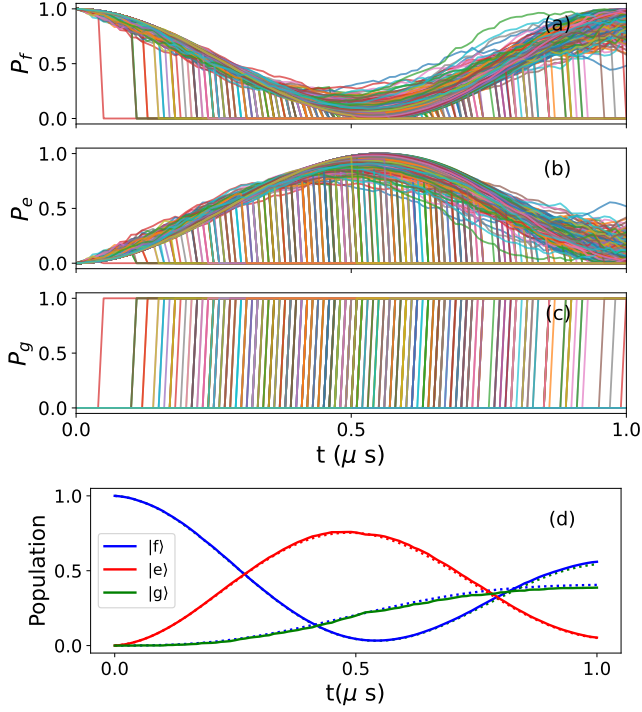


FIG. 2. (a)–(c) State-update trajectories obtained from Eq. (6). The trajectories are shown in terms of the state populations  $P_f$ ,  $P_e$ , and  $P_g$ , corresponding to the second excited, first excited, and ground states, respectively. These populations are the diagonal elements of the density matrix. (b) The ensemble-averaged values of the populations are shown as dotted lines. This ensemble average is compared with the average dynamics of the full three-level system, shown as dashed lines. The two averages match excellently. Parameters used:  $\gamma_g = 1$  MHz,  $\gamma_e = 0.2$  MHz, and  $\omega = 3$  MHz, with the number of trajectories =  $10^3$ .

From this measurement, only the outcomes that remain in the  $|e\rangle$  and  $|f\rangle$  manifold are considered for analysis. The two measurement schemes discussed above illustrate different unraveling models of the measurement trajectories of the three-level system. These unravelings yield the same average dynamics as obtained in a typical experimental measurement. When quantum jumps to the ground state are postselected and removed from the analysis, the resulting dynamics correspond to a non-Hermitian qubit.

### III. NON-HERMITIAN QUBIT

A non-Hermitian qubit is an isolated two-level system that interacts with a lossy or gain channel, or with both. The system evolves unitarily under an effective non-Hermitian Hamiltonian that accounts for the interaction with these channels. The qubit can separately un-

dergo spontaneous emission or fluorescence. Such a non-Hermitian fluorescent qubit can be modeled using the measurement scheme of a three-level system discussed in the previous section. This is achieved by post-selecting the trajectories from the detector measurements in which no jump from  $|e\rangle$  to  $|g\rangle$  has occurred. These trajectories include homodyne measurements of the  $|f\rangle \rightarrow |e\rangle$  spontaneous decay as well as decay into the non-Hermitian lossy channel at the rate  $\gamma_g$ . By averaging over all such trajectories, one can model a non-Hermitian fluorescent qubit, where the qubit is formed within the  $|f\rangle$  and  $|e\rangle$  manifold. The average dynamics of such a non-Hermitian qubit, especially close to the exceptional point (EP) where the eigenstates coalesce, can be studied through the formalism of the Liouvillian superoperator. Later, we compare the dynamics obtained from this approach with those obtained from the post-selected average trajectory approach.

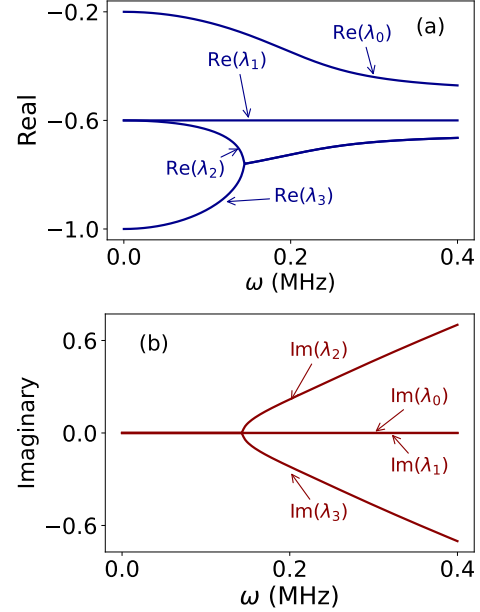


FIG. 3. Eigenvalue spectrum of the Liouvillian, with the real part shown in (a) and the imaginary part shown in (b). Parameters used:  $\gamma_g = 1$  MHz,  $\gamma_e = 0.2$  MHz.

As shown in the Appendix B, the differential equation for the vectorized density matrix  $\rho = (\rho_{ee}, \rho_{ef}, \rho_{fe}, \rho_{ff})^T$  of the  $|f\rangle$  and  $|e\rangle$  manifold can be written in the form  $\frac{d\rho}{dt} = \mathcal{L}\rho$ , where the Liouvillian operator  $\mathcal{L}$  is given by

$$\mathcal{L} = \begin{bmatrix} -\gamma_e & i\omega & -i\omega & \gamma_f \\ i\omega & -(\gamma_e + \gamma_g)/2 & 0 & -i\omega \\ -i\omega & 0 & -(\gamma_e + \gamma_f)/2 & i\omega \\ 0 & -i\omega & i\omega & -\gamma_f \end{bmatrix}. \quad (7)$$

The Liouvillian has four eigenvectors, and therefore the density operator can be expressed in terms of its eigen-

value decomposition as

$$\rho(t) = \sum_{k=1}^4 C_k e^{\lambda_k t} R_k, \quad (8)$$

where  $\lambda_k$  and  $R_k$  are the eigenvalues and right eigenvectors of  $\mathcal{L}$ , and  $C_k = \text{Tr}[L_k \rho(0)]$  are determined from the initial condition  $\rho(0)$ . The left and right eigenvectors satisfy the biorthonormal condition  $\text{Tr}[L_j R_k] = \delta_{jk}$ . The real parts of the eigenvalues are always negative [22], and hence they lead to relaxation of any observable toward the steady state. The imaginary parts, on the other hand, lead to oscillations in the observables. The spectrum of eigenvalues as a function of the drive strength  $\omega$  is shown in Fig. 3. As seen in the figure, we observe a second-order EP. On the right side of the EP, the imaginary parts are nonzero, resulting in oscillatory behavior of observables. Simultaneously, the real parts are negative and nonzero, which leads to decoherence at a rate proportional to the difference between the eigenvalues [20]. On the left of the EP, there are no oscillations, only decay. Therefore, the EP separates the overdamped and underdamped oscillatory regimes of the qubit.

#### IV. COMPARING AVERAGE DYNAMICS OF LIOUVILLIAN AND TRAJECTORY APPROACHES

In Fig. 6, we plot the normalized population of the  $|f\rangle$  state, defined as  $\rho_{ff}(t) \rightarrow \frac{\rho_{ff}(t)}{\rho_{ff}(t) + \rho_{ee}(t)}$ , for drive strengths both close to and far away from the exceptional point (EP). In the same figure, we compare this quantity with the ensemble-averaged  $\rho_{ff}$  obtained from trajectories that do not undergo a quantum jump to the  $|g\rangle$  state. Note that both homodyne and jump updates, as defined in Eq. (6), are used to generate the postselected “no-jump” trajectories. We do the comparison for two driving configurations: one where the qubit is driven about the  $x$ -axis and another where it is driven about the  $y$ -axis of the Bloch sphere. The corresponding measurement record is given by  $r = (x \cos \theta - y \sin \theta) \sqrt{\gamma_e} + \zeta(t)$ , as detailed in Appendix C. Depending on the measurement quadrature, we set  $\theta = 0$  (measurement along the  $x$ -axis) or  $\theta = \pi/2$  (measurement along the  $y$ -axis). In both cases, the Liouvillian-averaged dynamics agree closely with the ensemble-averaged trajectory results, whether the system is driven about the  $x$ - or  $y$ -axis. Figure 4 shows the results for  $\theta = 0$  for both drive configurations at two drive strengths, one close to the EP and the other far from it. Away from the EP, we observe more pronounced oscillations since the non-Hermitian decay rate  $\gamma_g$  is smaller than or comparable to the unitary drive strength. As the drive approaches the EP, non-Hermitian decay dominates over the unitary dynamics, leading to underdamped oscillations of the qubit. In this regime, quantum jumps from  $|e\rangle$  to  $|g\rangle$  occur more frequently. This explains the small deviation observed between the trajectory-based

and Liouvillian results near the EP, which becomes more pronounced when the qubit is driven about the  $y$ -axis at  $\theta = 0$ , and similarly, when driven about the  $x$ -axis at  $\theta = \pi/2$ .

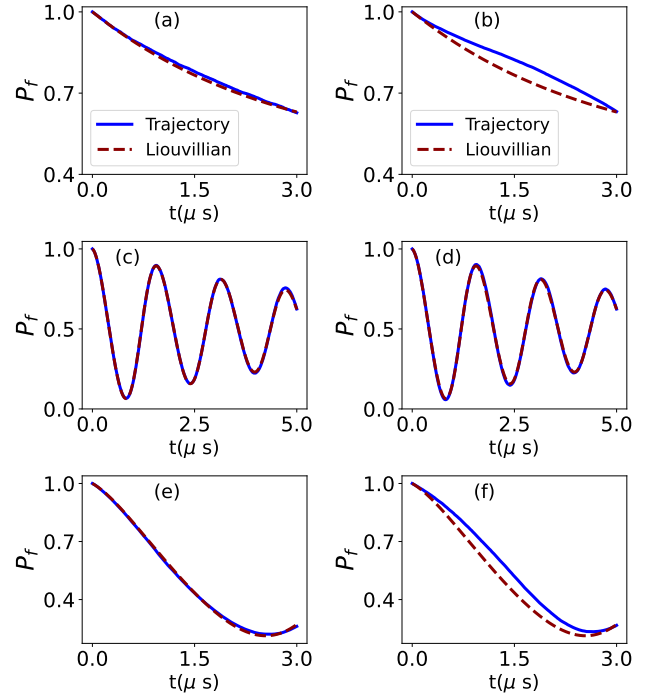


FIG. 4. The evolution of the normalized  $\rho_{ff}$  element of the density matrix, i.e., the population of the  $|f\rangle$  state ( $P_f$ ). The solid line corresponds to the result obtained from averaging the trajectories where both jump and no-jump state updates are considered, while the dotted line corresponds to the Liouvillian dynamics. (a)–(b) and (e)–(f) show the case where the drive strength is close to the Liouvillian EP, and (c)–(d) correspond to the case away from the EP. (a), (c) and (e) correspond to driving about the  $x$ -axis, while (b), (d) and (f) correspond to driving about the  $y$ -axis. All plots are generated at  $\theta = 0$ . A similar behavior is observed when  $\theta = \pi/2$ , except that in this case the  $x$ -axis drive resembles (b) and (f), while the  $y$ -axis drive resembles (a) and (e). Parameters used: for (a) and (b),  $\omega = 0.3$  MHz, for (c) and (d),  $\omega = 2$  MHz, and for (d) and (e)  $\omega = 0.7$ . The common parameters are  $\gamma_e = 0.2$  MHz and  $\gamma_g = 1$  MHz. The number of trajectories used is  $10^4$  and the time step is  $dt = 0.01\mu\text{s}$ .

#### V. TRAJECTORY ANALYSIS.

The Stratonovich form of the state update for the no-jump case ( $\rho(t+dt)_H$ ), given in Eq. 6 at  $\theta = 0$  (see Appendix A), is as follows. For the  $x$ -axis drive:

$$\begin{aligned} \dot{x} &= \frac{\gamma}{2} xz + r\sqrt{\gamma_e}(1+z-x^2), \\ \dot{y} &= \frac{\gamma}{2} yz - 2\omega z - r\sqrt{\gamma_e}xy, \\ \dot{z} &= \frac{\gamma}{2}(z^2 - 1) + 2\omega y - r\sqrt{\gamma_e}x(z+1), \end{aligned} \quad (9)$$

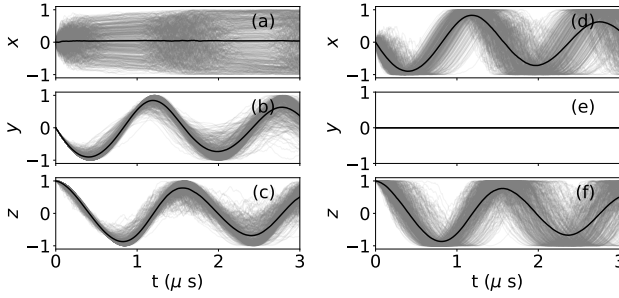


FIG. 5. Trajectory evolution of the Bloch vector components  $x$ ,  $y$ , and  $z$  of the non-Hermitian qubit at  $\theta = 0$ . (a)–(c) The qubit is driven about the  $x$ -axis. The mean of the trajectories is shown as a solid black curve. The qubit, initialized in the excited state, undergoes unitary oscillations about the  $x$ -axis. This evolution drives the  $y$  and  $z$  components, leading to oscillations. Due to the measurement backaction associated with the  $z$  evolution, the  $x$  component trajectories also fluctuate, although their mean remains zero. (d)–(f) The qubit is driven about the  $y$ -axis. Here the  $x$  and  $z$  components oscillate unitarily, while the  $y$  component remains zero. This is because the qubit starts in the excited state ( $z = 1$ ,  $x = 0$ ,  $y = 0$ ), and the backaction on the  $y$  evolution is independent of  $z$ , leaving  $y$  unchanged. For  $\theta = \pi/2$  measurements, the  $y$ -axis drive resembles the dynamics in (a)–(c), while the  $x$ -axis drive resembles those in (d)–(f); i.e., the roles are reversed. The common parameters used are  $\gamma_g = 1$  MHz and  $\gamma_e = 0.2$  MHz. The drive frequency is set to  $\omega = 2$  MHz.

For the y-axis drive:

$$\begin{aligned} \dot{x} &= 2\omega z + \frac{\gamma}{2} xz + r\sqrt{\gamma_e}(1 + z - x^2), \\ \dot{y} &= \frac{\gamma}{2} yz - r\sqrt{\gamma_e}xy, \\ \dot{z} &= \frac{\gamma}{2}(z^2 - 1) - 2\omega x - r\sqrt{\gamma_e}x(z + 1), \end{aligned} \quad (10)$$

where  $\gamma = \gamma_e - \gamma_g$  and the measurement record is  $r = \sqrt{\gamma_e}x + \zeta(t)$ , with  $\zeta(t)$  being Gaussian white noise of zero mean and variance  $1/dt$ . The non-Hermitian decay  $\gamma_g$  appears only in the drift term of the equations, while measurement backaction is determined by the characteristic measurement time  $T_e = 1/\gamma_e$ . We observe that in the x-axis drive, the differential equations for all Bloch vector components  $x$ ,  $y$ , and  $z$  are interdependent, whereas in the y-axis drive, the evolution of  $x$  and  $z$  is independent of  $y$ . This can be seen from the trajectory plots of Eqs. (9) and (10), shown in Fig. 5. In the y-axis drive, the evolution of  $x$  and  $z$  has no contribution from the  $y$  component, and if the system is initially in the  $|f\rangle$  state,  $y$  remains zero. In contrast, for the x-axis drive, the evolutions of all components are coupled, and the evolution in  $x$  contributes to the evolution of  $y$  and  $z$  in the form of measurement backaction. This leads to different ensemble-averaged values for the x- and y-axis drives near the EP, with the x-axis drive closely matching the Liouvillian evolution as shown in Fig. 6. The  $y$  drive departs from the Liouvillian approach significantly and even retains some oscillation. When the drive strength is

much larger than the non-Hermitian decay, both drives reproduce the Liouvillian behavior, as the unitary evolution dominates over the non-Hermitian part.

When we record the measurement of the  $y$  component, i.e.,  $r = -\sqrt{\gamma_e}y + \zeta(t)$  for  $\theta = \pi/2$ , the roles reverse. In this case, the  $y$ -axis drive differential equations depend on all Bloch vector components, whereas in the  $x$ -axis drive, the evolution of  $y$  and  $z$  remains independent of  $x$ . Applying the same reasoning as before, the  $y$ -axis drive closely reproduces the Liouvillian evolution, while the  $x$ -axis drive does not. Again, when the unitary drive dominates over the non-Hermitian decay, both drives reproduce the Liouvillian behavior.

In the absence of the non-Hermitian loss channel, i.e.,  $\gamma_g = 0$ , the dynamics of the qubit in the  $|f\rangle$  and  $|e\rangle$  manifold match in both the Liouvillian and the trajectory approach, irrespective of the drive type and measurement record, as shown in Fig. 7. It is only in the presence of  $\gamma_g$  that the dynamics differ. Therefore, we observe that the interplay between the non-Hermitian lossy channel ( $\gamma_g$ ) and the type of measurement record  $r$  can produce different dynamics of a non-Hermitian qubit, where a particular drive and measurement record give an approximately similar dynamics as the Liouvillian approach, but different combinations lead to different dynamics.

The two Eqs. (10) and (9) can be derived from the normalized Itô stochastic master equation

$$\begin{aligned} d\rho = & -i[H, \rho] dt - \frac{\gamma_g}{2} \{ |e\rangle \langle e|, \rho \} dt + \gamma_e \mathcal{D}[|e\rangle \langle f|] \rho dt \\ & + \gamma_g \langle |e\rangle \langle e| \rangle \rho dt + \sqrt{\gamma_e} \mathcal{H}[|e\rangle \langle f| e^{i\theta}] \rho dW, \end{aligned} \quad (11)$$

provided it is interpreted in the Stratonovich sense. The average dynamics obtained by simply assuming  $\langle \rho(t), dW(t) \rangle = 0$  in Eq. 11 (Liouvillian approach) do not coincide with those obtained by ensemble averaging the trajectories from the Stratonovich evolution, or equivalently, with the averaged trajectory dynamics from the Itô stochastic differential equation derived from Eq. 11. In other words, the ensemble average of trajectories of the Itô form does not match the Liouvillian dynamics, especially when the non-Hermitian decay rate  $\gamma_g$  is much larger than the unitary evolution frequency  $\omega$ . When  $\gamma_g = 0$ , the normalization term  $\gamma_g \langle |e\rangle \langle e| \rangle \rho dt$  and the non-Hermitian term  $-\frac{\gamma_g}{2} \{ |e\rangle \langle e|, \rho \} dt$  vanish, allowing one to take the approximation  $\langle \rho(t) dW(t) \rangle = 0$ . This then reproduces the same dynamics as the trajectory approach. Therefore, the non-Hermitian decay channel introduces an extra backaction that becomes evident only when considering the trajectory average. Due to the non-Hermitian decay channel arising from post-selection, there is measurement-induced backaction on the system such that the noise becomes correlated with the system's state.

The state updates given by Eq. (9), Eq. (10), and Eq. (11) correspond to the case where the jump update  $\rho(t+dt)_J$  is not included. The trajectories obtained from these equations therefore also contain those that could have undergone a jump to the  $|g\rangle$  manifold. To accu-

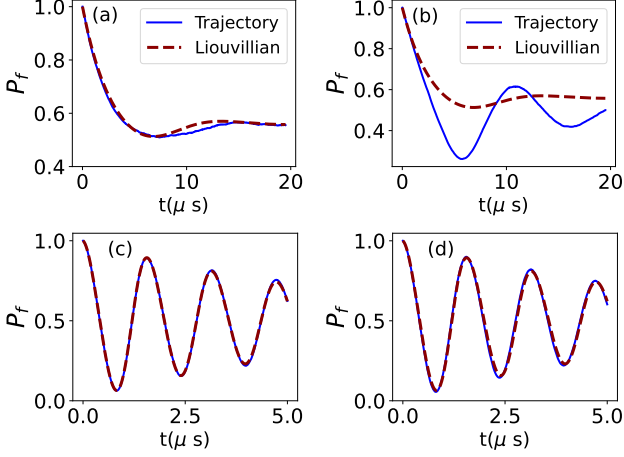


FIG. 6. The evolution of the normalized  $\rho_{ff}$  element of the density matrix, i.e., the population of the  $|f\rangle$  state ( $P_f$ ). The solid line corresponds to the result obtained from averaging only the jump state-update trajectories, while the dotted line corresponds to the Liouvillian dynamics. (a)–(b) show the case where the drive strength is close to the Liouvillian EP, and (c)–(d) correspond to the case away from the EP. (a) and (c) correspond to driving about the  $x$ -axis, while (b) and (d) correspond to driving about the  $y$ -axis. All plots are generated at  $\theta = 0$ . A similar behavior is observed when  $\theta = \pi/2$ , except that in this case the  $x$ -axis drive resembles (b), while the  $y$ -axis drive resembles (a). Parameters used: for (a) and (b),  $\omega = 0.3$  MHz, and for (c) and (d),  $\omega = 2$  MHz. The common parameters are  $\gamma_e = 0.2$  MHz and  $\gamma_g = 1$  MHz.

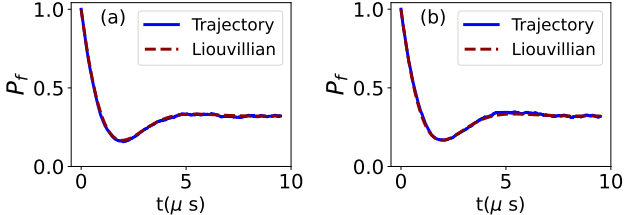


FIG. 7. Comparison of the trajectory average and the Liouvillian average in terms of the  $|f\rangle$  state population for the case when the non-Hermitian loss rate is  $\gamma_g = 0$ . (a) corresponds to driving about the  $x$ -axis, and (b) corresponds to driving about the  $y$ -axis. Irrespective of the drive axis, both averages are identical. The parameters used are  $\gamma_e = 1$  MHz,  $\gamma_g = 0$  MHz, and  $\omega = 0.3$  MHz.

rately capture the dynamics of the non-Hermitian qubit, both the no-jump update  $\rho(t+dt)_H$  and the jump update  $\rho(t+dt)_J$  must be included. After applying both updates, we postselect the trajectories that have not decayed to the ground-state manifold and perform the ensemble averaging over this subset. The ensemble-averaged dynamics that include both the jump and no-jump updates are shown in Fig. 4, while the dynamics obtained using only the no-jump update are shown in Fig. 6. Comparing the two results, we find that for drive strengths far from the EP, both approaches yield nearly identical results. In

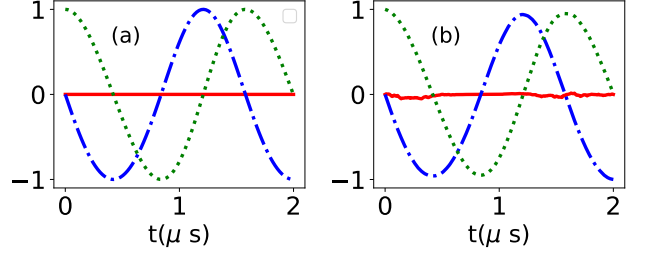


FIG. 8. (a) shows the ensemble-averaged trajectory, while (b) shows the path obtained from the extremization of the action for the  $x$ -axis drive. The dashed red, dash-dotted blue, and dotted green curves correspond to the Bloch vector components  $x$ ,  $y$ , and  $z$ , respectively. The postselected state is  $q_f = [0, -1, 0]$ . The common parameters used are  $\gamma_g = 1$  MHz and  $\gamma_e = 0.2$  MHz, with the drive frequency set to  $\omega = 2$  MHz.  $\lambda = 0.05$

this regime, the unitary drive dominates over the jump probability, which depends on the non-Hermitian decay rate  $\gamma_g$ . Consequently, only a small fraction of trajectories decay to the ground state within the timescale of the unitary evolution. Near the EP, however, the dynamics deviate significantly when the qubit is driven about the  $y$ -axis, while the agreement remains good for drives about the  $x$ -axis at  $\theta = 0$ . As the drive approaches the EP, the decay rate  $\gamma_g$  dominates over the unitary drive strength, causing a larger number of trajectories to collapse into the ground state. As a result, the ensemble-averaged dynamics differ between the two approaches in this regime. The fact that the deviation is more significant for the  $y$ -axis drive and less pronounced for the  $x$ -axis drive can be understood from the trajectory analysis discussed above. When the measurement is performed at  $\theta = \pi/2$ , the situation reverses — the  $x$ -axis drive shows noticeable deviation, while the  $y$ -axis drive agrees well with the Liouvillian dynamics.

## VI. OPTIMAL PATH.

Every trajectory has an associated action, similar to the action in the path integral formalism. The exponential of the action determines the probability of evolving from an initial state to a final state. The action for each trajectory is defined as [47, 48]

$$S = \int_0^T dt \left( -p \cdot \dot{q} + \mathcal{H}(q, p, r) \right), \quad (12)$$

where  $\mathcal{H}(q, p, r)$  is the Hamiltonian (see Appendix D). Here,  $q = [x, y, z]$  are the Bloch components,  $p$  is the conjugate momentum, and  $r$  is the measurement record.

By extremizing the action, i.e., setting  $\delta S = 0$ , we obtain a set of constraint equations that define the optimal path of the trajectories. Given an initial state  $q_i$  and a final state  $q_f$ , the optimal paths for  $\sigma_x$  drive with  $\theta = 0$  is shown in Fig. 8. We also compare the optimal path with

the trajectory obtained by averaging postselected trajectories. The trajectories are postselected by imposing the condition  $|q_n - q_f| < \lambda$ , where  $\lambda$  is a tolerance parameter less than unity. As shown in Fig. 8, the postselected average trajectory matches the optimal path obtained from extremizing the action.

We can further perform a one-dimensional phase-space analysis of the qubit optimal path. By substituting  $y = 0$ ,  $x = \sin \theta$ , and  $z = \cos \theta$  into the optimal path equation for the  $y$ -axis drive under  $y$ -vector measurement of the qubit, we can confine the qubit dynamics to the  $x$ - $z$  plane of the Bloch sphere (see Appendix D). Note that this  $\theta$  is different from the phase difference  $\theta$  used for measurement. The paths corresponds to a pure state, with  $\theta = 0 \rightarrow |e\rangle$  and  $\theta = \pi \rightarrow |f\rangle$ . The corresponding Hamiltonian  $\mathcal{H}(\theta, p)$  (see Appendix D) is a constant of motion  $E$  along the optimal path. Consequently, one can plot the conjugate momentum  $p(\theta, E)$  to visualize the qubit optimal trajectory in phase space. The phase portrait for different energy constants is shown in Fig. 9. Compared to a generic two-level system, the non-Hermitian two-level system exhibits a similar phase-space structure [25, 52]. In the non-Hermitian case, the fixed points positions are shifted. Of all the paths that start from a particular state  $q_i$ , the one that ends at  $p_f = 0$  extremizes the action.

## VII. CONCLUSION.

In summary, we have investigated a homodyne measurement of a two-level non-Hermitian qubit realized through post-selection of a three-level superconducting qubit system. The post-selection procedure, which discards quantum jump to the ground-state manifold  $|g\rangle$  while retaining excitations in the  $|e\rangle$  and  $|f\rangle$  manifolds, effectively generates a non-Hermitian qubit exhibiting  $\mathcal{PT}$  symmetry. Building on this framework, we have analyzed the system under continuous homodyne measurement during spontaneous emission, thereby probing the interplay between non-Hermitian decay and measurement backaction. Our results show that, the no-jump stochastic differential equation describing the post-selected non-Hermitian qubit agree with those of the jump-updated postselected or Liouvillian evolution at drive strengths far from the Liouvillian exceptional point (EP). The degree of deviation near the EP depends sensitively on the nature of the drive, with qualitative differences depending on whether the qubit is driven about the  $x$ - or  $y$ -axis of the Bloch sphere. Furthermore, by employing a path-integral formulation within the quantum trajectory approach, we identified the most likely measurement paths under post-selection. These findings highlight how measurement backaction and non-Hermitian dynamics together shape the transient behavior of open quantum systems, and they provide a pathway for exploring controlled dynamics near exceptional points.

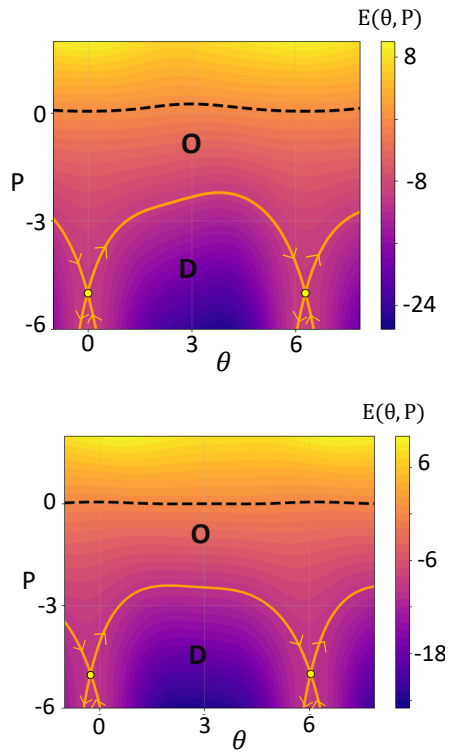


FIG. 9. Phase-space plots of the qubit's optimal paths for different values of the energy constant  $E(\theta, p)$ . **(Top)** For  $\omega = 2$  MHz and  $\gamma_g = 1$  MHz, two saddle fixed points are observed at  $(\theta, p) = (0.0, -0.65)$  and  $(2\pi, -0.65)$ , indicated by yellow circles. The separatrix (gold line) corresponds to trajectories crossing the fixed point. In the region labeled **O**, the paths oscillate between  $\theta = 0$  ( $|e\rangle$ ) and  $\theta = 2\pi$  ( $|f\rangle$ ). The black dotted curve denotes a trajectory crossing the  $p = 0$  line. In region **-C**, trajectories approach  $\theta = \pi$  ( $|e\rangle$ ) in the clockwise direction, while in region **-A**, they tend toward  $|e\rangle$  in the counterclockwise direction. **(Bottom)** For  $\omega = 2$  MHz and  $\gamma_g = 0$  MHz, the fixed points are shifted. This corresponds to a generic two level system in the  $|f\rangle$  and  $|e\rangle$  manifold. Common parameters:  $\gamma_e = 0.2$  MHz.

## ACKNOWLEDGEMENT

This work is supported by MoE, Government of India (Grant No. MoE-STARS/STARS-2/2023-0161).

## Appendix A: Average Dynamics of the Three-Level System

The state of the three-level system under the hybrid detection protocol updates at each measurement interval

$dt$  as [33]

$$\begin{aligned} d\rho = & -i[H, \rho] dt - \frac{\gamma_g}{2} \{ |e\rangle \langle e|, \rho \} dt + \gamma_g \langle e \rangle \langle e | \rho dt \\ & + \left( \frac{|g\rangle \langle e| \rho |e\rangle \langle g|}{\langle |e\rangle \langle e|} - \rho \right) dN + \gamma_e \mathcal{D}[|e\rangle \langle f|] \rho dt \\ & + \sqrt{\gamma_e} \mathcal{H}[|e\rangle \langle f| e^{i\theta}] \rho dW, \end{aligned} \quad (\text{A1})$$

where,  $H$  is the unitary Hamiltonian of the system and

$$\begin{aligned} \mathcal{H}[|e\rangle \langle f| e^{i\theta}] \rho = & e^{i\theta} |e\rangle \langle f| \rho + e^{-i\theta} \rho |f\rangle \langle e| \\ & - \langle e^{i\theta} |e\rangle \langle f| + e^{-i\theta} |f\rangle \langle e| \rangle \rho, \end{aligned} \quad (\text{A2})$$

with  $dW$  being a Wiener process having zero mean,  $\langle dW(t) \rangle = 0$ , and  $dW(t)^2 = dt$ . The term  $dN$  defines the counting process where, during the interval  $dt$ , it takes the value unity with probability  $\gamma_g \langle e \rangle \langle e | dt$  and zero otherwise. The above equation is a stochastic master equation in Itô form. To obtain the ensemble-averaged dynamics of the system, we take the average  $\langle d\rho \rangle$ , which yields

$$\frac{d\rho}{dt} = -i[H, \rho] + \gamma_g \mathcal{D}[|g\rangle \langle e|] \rho + \gamma_e \mathcal{D}[|e\rangle \langle f|] \rho, \quad (\text{A3})$$

where  $\langle \rho dN \rangle = \gamma_g \langle \rho |e\rangle \langle e| \rangle dt$  is used. Here, we have rewritten  $\langle \rho(t) \rangle \rightarrow \rho(t)$  for simplicity.

The ensemble evolution of the system from Eq. (A3) can be mapped onto the one derived by taking the ensemble average of the trajectories discussed in the main text. To numerically simulate the trajectories, we compute the relative probabilities of whether the  $|e\rangle \rightarrow |g\rangle$  jump is registered in the detector or not. The jump is registered with probability  $P_J = \text{tr}(K_J \rho(t) K_J^\dagger)$ , and no jump occurs with probability  $P_H = \text{tr}(K_H \rho(t) K_H^\dagger)$ . In the case of no jump, the homodyne record  $r$  is inferred from a Gaussian distribution with mean  $\sqrt{\gamma_e} ((\rho_{ef} e^{i\theta} + \rho_{fe} e^{-i\theta}) / (\rho_{ff} + \rho_{ee} + \rho_{gg}))$ . The two probabilities are normalized and a multinomial distribution is sampled, with outcome 0 corresponding to no jump and outcome 1 corresponding to a jump. Whenever the outcome is 0, the system state is updated using  $\rho_H(t+dt)$ , and when the outcome is 1, it is updated using  $\rho_J(t+dt)$  (see Eq. (6)).

The Kraus operators  $K_H$  and  $K_J$  are obtained from the relations  $K_H = \langle X | M | E_0 \rangle$  and  $K_J = \langle E_{1g} | M | E_0 \rangle$ , where the homodyne measurement record  $X = r \sqrt{dt/2}$  and the projections are given by

$$\langle X | E_0 \rangle = \left( \frac{1}{\pi} \right)^{1/4} e^{-X^2/2}, \quad (\text{A4})$$

$$\langle X | E_{1e} \rangle = \left( \frac{1}{\pi} \right)^{1/4} e^{-X^2/2} \sqrt{2} X, \quad (\text{A5})$$

$$\langle X | E_{1g} \rangle = 0. \quad (\text{A6})$$

In the Kraus operator  $K_J$ , the Gaussian noise signal with zero mean, induced from the homodyne counterpart, is included [52].

## Appendix B: Liouvillian of the Post-Selected $|f\rangle$ and $|e\rangle$ manifold qubit.

The Itô form of the stochastic master equation for the three-level system, where jumps from the  $|e\rangle$  to  $|g\rangle$  state are removed using post-selection, is given from Eq. (A1) as

$$\begin{aligned} d\rho = & -i[H, \rho] dt - \frac{\gamma_g}{2} \{ |e\rangle \langle e|, \rho \} dt + \gamma_e \mathcal{D}[|e\rangle \langle f|] \rho dt \\ & + \sqrt{\gamma_e} \mathcal{H}[|e\rangle \langle f| e^{i\theta}] \rho dW, \end{aligned} \quad (\text{B1})$$

where the normalization factor (the third term in Eq. (B1)) is not taken into account. By taking the ensemble average of Eq. (B1), the unmonitored master equation for the fluorescent non-Hermitian qubit in the  $|f\rangle$ - $|e\rangle$  manifold can be written as

$$\frac{d\rho}{dt} = -i[H, \rho] - \frac{\gamma_g}{2} \{ |e\rangle \langle e|, \rho \} + \gamma_e \mathcal{D}[|e\rangle \langle f|] \rho. \quad (\text{B2})$$

We have assumed  $\langle \rho(t) dW(t) \rangle = 0$ . In terms of the Liouvillian operator, this can be written as

$$\frac{d\rho}{dt} = \mathcal{L} \rho, \quad (\text{B3})$$

where  $\rho = (\rho_{ff}, \rho_{fe}, \rho_{ef}, \rho_{ee})^T$  and

$$\begin{aligned} \mathcal{L} = & -i(H \otimes I - I \otimes H^T) - \frac{\gamma_g}{2} |e\rangle \langle e| \otimes I - \frac{\gamma_g}{2} I \otimes |e\rangle \langle e| \\ & - \frac{\gamma_e}{2} |f\rangle \langle f| \otimes I - \frac{\gamma_e}{2} I \otimes |f\rangle \langle f| + \gamma_e |e\rangle \langle f| \otimes |e\rangle \langle f|, \end{aligned} \quad (\text{B4})$$

resulting in the matrix form given in Eq. (7). The normalized population  $\rho_{ff}(t) \rightarrow \frac{\rho_{ff}(t)}{\rho_{ff}(t) + \rho_{ee}(t)}$  obtained by solving Eq. B3 can also be obtained by solving the normalized Itô master equation

$$\begin{aligned} d\rho = & -i[H, \rho] dt - \frac{\gamma_g}{2} \{ |e\rangle \langle e|, \rho \} dt + \gamma_e \mathcal{D}[|e\rangle \langle f|] \rho dt \\ & + \gamma_g \langle e | \rho dt. \end{aligned} \quad (\text{B5})$$

## Appendix C: State Update of the Post-Selected trajectories.

The state update of the system when no jump is registered in the detector is given by

$$\rho(t+dt)|_H = \frac{U K_H \rho(t) K_H^\dagger U^\dagger}{\text{tr}(U K_H \rho(t) K_H^\dagger U^\dagger)}, \quad (\text{C1})$$

where  $U = \exp(-i\omega(|f\rangle \langle f| + |e\rangle \langle e|)dt)$  for the x-axis drive, and  $U = \exp(-i\omega(-i|f\rangle \langle e| + i|e\rangle \langle f|)dt)$  for the y-axis drive. By expanding the Kraus and unitary operators up to first order in  $dt$ , the state update can be written as

$$\frac{\rho(t+dt) - \rho(t)}{dt} = i[\rho, H] + (\Sigma \rho + \rho \Sigma^\dagger) - \rho \text{tr}(\Sigma \rho + \rho \Sigma^\dagger), \quad (\text{C2})$$

where

$$\Sigma = \begin{bmatrix} -\frac{r^2}{4} - \frac{\gamma_e}{2} & 0 & 0 \\ \sqrt{\gamma_e}r & -\frac{r^2}{4} - \frac{\gamma_g}{2} & 0 \\ 0 & 0 & -\frac{r^2}{4} \end{bmatrix}. \quad (\text{C3})$$

Since the population of the system does not decay to the ground state (because no jump is registered), we consider only the  $|f\rangle-|e\rangle$  manifold. The last term of Eq. (C2) can be written as

$$\begin{aligned} \rho \text{Tr}(\Sigma\rho + \rho\Sigma^\dagger) &= \rho_{ff}(-r^2/2 - \gamma_e) + \rho_{ee}(-r^2/2 - \gamma_g) \\ &+ \rho_{gg}(-r^2/2) + \rho_{ef}\sqrt{\gamma_e}r + \rho_{fe}\sqrt{\gamma_e}r. \end{aligned} \quad (\text{C4})$$

Expanding Eq. (C2), we obtain the differential equations for the  $|f\rangle-|e\rangle$  manifold, namely  $\dot{\rho}_{ff}$ ,  $\dot{\rho}_{ee}$ ,  $\dot{\rho}_{fe}$ , and  $\dot{\rho}_{ef}$ . In these equations, the contribution from the  $|g\rangle$  state appears through  $\rho_{gg}$  in Eq. (C4). Considering that the qubit starts in the  $|f\rangle$  state, we postselect those trajectories that do not decay to the ground state  $|g\rangle$ . This postselection condition effectively enforces  $\rho_{gg} = 0$  throughout the evolution of the  $|f\rangle-|e\rangle$  postselected trajectories. Then, in terms of the Bloch vector components  $x$ ,  $y$ , and  $z$  used to represent a typical two-level system, the update equation in Stratonovich form can be written using Eq. (C1) as follows: For the x-axis drive, i.e.,  $H = \omega(|f\rangle\langle e| + |e\rangle\langle f|)$ :

$$\begin{aligned} \dot{x} &= \frac{\gamma}{2}xz + r\sqrt{\gamma_e}[(1+z-x^2)\cos\theta + xy\sin\theta], \\ \dot{y} &= \frac{\gamma}{2}yz - 2\omega z + r\sqrt{\gamma_e}[(y^2-z-1)\sin\theta - xy\cos\theta], \\ \dot{z} &= \frac{\gamma}{2}(z^2-1) + 2\omega y + r\sqrt{\gamma_e}(y\sin\theta - x\cos\theta)(z+1), \end{aligned} \quad (\text{C5})$$

For the y-axis drive, i.e.,  $H = \omega(-i|f\rangle\langle e| + i|e\rangle\langle f|)$ :

$$\begin{aligned} \dot{x} &= 2\omega z + \frac{\gamma}{2}xz + r\sqrt{\gamma_e}[(1+z-x^2)\cos\theta + xy\sin\theta], \\ \dot{y} &= \frac{\gamma}{2}yz + r\sqrt{\gamma_e}[(y^2-z-1)\sin\theta - xy\cos\theta], \\ \dot{z} &= \frac{\gamma}{2}(z^2-1) - 2\omega x + r\sqrt{\gamma_e}(y\sin\theta - x\cos\theta)(z+1), \end{aligned} \quad (\text{C6})$$

where  $\gamma = \gamma_e - \gamma_g$ . The measurement record  $r$  can be inferred from the probability  $P = \text{tr}(UK_H\rho(t)K_H^\dagger U^\dagger)$ , which, when expanded to first order in  $dt$ , becomes

$$\begin{aligned} P &= \exp\left[\frac{dt}{2}((x\cos\theta - y\sin\theta)^2\gamma_e \right. \\ &\quad \left. - \frac{1+z}{2}\gamma_e - \frac{1-z}{2}\gamma_g)\right]\sqrt{N} \\ &\times \exp\left[-\frac{dt}{2}(r - \sqrt{\gamma_e}(x\cos\theta - y\sin\theta))^2\right]. \end{aligned} \quad (\text{C7})$$

This shows that the probability density is Gaussian in  $r$  with variance  $1/dt$  and mean  $\sqrt{\gamma_e}(x\cos\theta - y\sin\theta)$ . Therefore, we can write

$$r = \sqrt{\gamma_e}(x\cos\theta - y\sin\theta) + \zeta(t), \quad (\text{C8})$$

where the noise term  $\zeta(t)$  is Gaussian with zero mean and variance  $1/dt$ . The two Eqs. (C5) and (C6) can be derived from the normalized Itô stochastic master equation

$$\begin{aligned} d\rho &= -i[H, \rho]dt - \frac{\gamma_g}{2}\{|e\rangle\langle e|, \rho\}dt + \gamma_e\mathcal{D}[|e\rangle\langle f|]\rho dt \\ &+ \gamma_g\langle|e\rangle\langle e|\rangle\rho dt + \sqrt{\gamma_e}\mathcal{H}[|e\rangle\langle f|e^{i\theta}]\rho dW, \end{aligned} \quad (\text{C9})$$

provided it is correctly interpreted in the Stratonovich form. The Itô form for  $\theta = 0$  is given by

$$\begin{aligned} dx &= \left(-\frac{\gamma_e}{2}x - \frac{\gamma_g}{2}xz\right)dt + \sqrt{\gamma_e}(1+z-x^2)dW, \\ dy &= \left(-2\omega z - \frac{\gamma_e}{2}y - \frac{\gamma_g}{2}yz\right)dt + \sqrt{\gamma_e}(-xy)dW, \\ dz &= \left(2\omega y - \gamma_e(1+z) + \frac{\gamma_g}{2}(1-z^2)\right)dt \\ &+ \sqrt{\gamma_e}(-x(1+z))dW, \end{aligned} \quad (\text{C10})$$

for the  $x$ -axis drive, and

$$\begin{aligned} dx &= \left(2\omega z - \frac{\gamma_e}{2}x - \frac{\gamma_g}{2}xz\right)dt + \sqrt{\gamma_e}(1+z-x^2)dW, \\ dy &= \left(-\frac{\gamma_e}{2}y - \frac{\gamma_g}{2}yz\right)dt + \sqrt{\gamma_e}(-xy)dW, \\ dz &= \left(-2\omega x - \gamma_e(1+z) + \frac{\gamma_g}{2}(1-z^2)\right)dt \\ &+ \sqrt{\gamma_e}(-x(1+z))dW, \end{aligned} \quad (\text{C11})$$

for the  $y$ -axis drive. By taking ensemble average of Eq. C9 or Eq. C10 and Eq. C11, and assuming  $\langle\rho(t)dW(t)\rangle = 0$ , we obtain the normalized population similar to the one obtained from Eq. B3, i.e., the Liouvillain dynamics.

#### Appendix D: Optimal Path Analysis.

Given an initial and final state of the non-Hermitian qubit, one can find the optimal path of the trajectories by extremizing the action  $S$  associated with the trajectories. The action for each trajectory is defined as

$$S = \int_0^T dt \left( -p \cdot \dot{q} + \mathcal{H}(q, p, r) \right), \quad (\text{D1})$$

where

$$\mathcal{H}(q, p, r) = p \cdot F[q, r] + G[q, r]. \quad (\text{D2})$$

Here,  $q = [x, y, z]$  are the Bloch components,  $p$  corresponds to the conjugate momentum, and  $r$  is the measurement record. The function  $F[q, r] = \dot{q}$  is given by Eqs. (C5) or (C6), and  $G[q, r] = \text{Tr}(\Sigma\rho + \rho\Sigma^\dagger)$ .

By extremizing the action, i.e., setting  $\delta S = 0$ , we obtain a set of constraint equations:

$$\begin{cases} \dot{q} = \frac{\partial \mathcal{H}}{\partial p}, \\ \dot{p} = -\frac{\partial \mathcal{H}}{\partial q}, \\ 0 = \frac{\partial \mathcal{H}}{\partial r}. \end{cases} \quad (\text{D3})$$

For the  $\sigma_y$  drive and  $\theta = 0$  measurement, we obtain the following equations for the Bloch vector:

$$\begin{aligned}\dot{x} &= 2\omega z + \frac{\gamma}{2}xz + r\sqrt{\gamma_e}(1+z-x^2), \\ \dot{y} &= \frac{\gamma}{2}yz + \sqrt{\gamma_e}(-xy)r, \\ \dot{z} &= -2\omega x + \frac{\gamma}{2}(z^2-1) + \sqrt{\gamma_e}(z+1)(-x)r.\end{aligned}\quad (\text{D4})$$

The conjugate momenta evolve as

$$\begin{aligned}\dot{p}_x &= -\left(p_x\left(\frac{\gamma}{2}z - 2r\sqrt{\gamma_e}x\right) + p_y(-\sqrt{\gamma_e}ry) + p_z(-2\omega - \sqrt{\gamma_e}r(z+1)) + r\sqrt{\gamma_e}r\right), \\ \dot{p}_y &= -\left(p_y\left(\frac{\gamma}{2}z - r\sqrt{\gamma_e}x\right)\right), \\ \dot{p}_z &= -\left(p_x(2\omega + \frac{\gamma}{2}x + r\sqrt{\gamma_e}) + p_y(\sqrt{\gamma_e}y) + p_z(\gamma z - r\sqrt{\gamma_e}) - \frac{\gamma}{2}\right).\end{aligned}\quad (\text{D5})$$

The optimal measurement record  $r$  is obtained self-consistently as

$$\begin{aligned}r &= p_x\sqrt{\gamma_e}(1+z-x^2) + p_y\sqrt{\gamma_e}(-xy) \\ &\quad + p_z\sqrt{\gamma_e}(z+1)(-x) + \sqrt{\gamma_e}x.\end{aligned}\quad (\text{D6})$$

Thus, one can numerically solve for  $x$ ,  $y$ , and  $z$  for arbitrary initial and final states by substituting the optimized  $r$  from Eq. (D6) into Eqs. (D4)–(D5) and obtain the corresponding optimal path.

We can perform a one-dimensional phase-space analysis of the qubit optimal path by substituting  $y = 0$ ,  $x = \sin \theta$ , and  $z = \cos \theta$ . Each trajectory corresponds to a pure state, with  $\theta = 0 \rightarrow |e\rangle$  and  $\theta = \pi \rightarrow |f\rangle$ . The optimal path equations then reduce to

$$r = p\sqrt{\gamma_e}(1 + \cos \theta) + \sqrt{\gamma_e} \sin \theta, \quad (\text{D7})$$

$$\dot{\theta} = 2\omega + \frac{\gamma}{2} \sin \theta + r\sqrt{\gamma_e}(1 + \cos \theta), \quad (\text{D8})$$

$$\dot{p} = -\left(p\left(\frac{\gamma}{2} \cos \theta - r\sqrt{\gamma_e} \sin \theta\right) + r\sqrt{\gamma_e} \cos \theta + \frac{\gamma}{2} \sin \theta\right). \quad (\text{D9})$$

The corresponding Hamiltonian can be written as

$$\mathcal{H} = A(\theta)p^2 + B(\theta)p + C(\theta), \quad (\text{D10})$$

with

$$\begin{aligned}A(\theta) &= \frac{\gamma_e}{2}(1 + \cos \theta)^2, \\ B(\theta) &= 2\omega + \left(\frac{3}{2}\gamma_e - \frac{\gamma_g}{2}\right) \sin \theta + \frac{\gamma_e}{2} \sin(2\theta), \\ C(\theta) &= \frac{\gamma_e}{2}(1 - \cos \theta) + \frac{\gamma_e}{4}(1 - \cos(2\theta)) \\ &\quad - \gamma_e - \frac{\gamma_g}{2}(1 - \cos \theta).\end{aligned}\quad (\text{D11})$$

This Hamiltonian  $\mathcal{H}$  is a constant of motion  $E$  for the optimal path. Consequently, one can plot the conjugate momentum  $p(\theta, E)$  to visualize the qubit optimal trajectory in phase space.

---

[1] C. M. Bender, Making sense of non-hermitian hamiltonians, *Reports on Progress in Physics* **70**, 947 (2007).

[2] C. M. Bender, S. Boettcher, and M. P. N. Pt-symmetric quantum mechanics, *J. Math. Phys.* **40**, 2201–2229 (1999).

[3] S. Croke, Pt-symmetric hamiltonians and their application in quantum information, *Phys. Rev. A* **91**, 052113 (2015).

[4] W. D. Heiss, The physics of exceptional points, *Journal of Physics A: Mathematical and Theoretical* **45**, 444016 (2012).

[5] M. A. Miri and A. Alu, Exceptional points in optics and photonics, *Science* **363**, eaar7709 (2019).

[6] S. Ozdemir, S. Rotter, F. Nori, and L. Yang, Parity-time symmetry and exceptional points in photonics, *Nature Material* **18**, 783–798 (2019).

[7] B. Peng, c. K. Ozdemir, F. Lei, F. Monifi, M. Gianfreda, G. L. Long, S. Fan, F. Nori, C. M. Bender, and L. Yang, Parity-time-symmetric whispering-gallery microcavities, *Nature Physics* **10**, 394 (2014).

[8] L. Feng, R. El-Ganainy, and L. Ge, Non-hermitian photonics based on parity-time symmetry, *Nature Photonics* **11**, 752 (2017).

[9] H. Hodaei, M.-A. Miri, M. Heinrich, D. N. Christodoulides, and M. Khajavikhan, Parity-time-symmetric microring lasers, *Science*, *Science* **346**, 975 (2014).

[10] J. M. Zeuner, M. C. Rechtsman, Y. Plotnik, Y. Lumer, S. Nolte, M. S. Rudner, M. Segev, and A. Szameit, Observation of a topological transition in the bulk of a non-hermitian system, *Phys. Rev. Lett.* **115**, 040402 (2015).

[11] L. Xiao, X. Zhan, Z. H. Bian, K. K. Wang, X. Zhang, X. P. Wang, J. Li, K. Mochizuki, D. Kim, N. Kawakami, W. Yi, H. Obuse, B. C. Sanders, and P. Xue, Observation of topological edge states in parity-time-symmetric quantum walks, *Nature Physics* **13**, 1117 (2017).

[12] B. Peng, S. K. Ozdemir, S. Rotter, H. Yilmaz, M. Liertzer, F. Monifi, C. M. Bender, F. Nori, and L. Yang, Loss-induced suppression and revival of lasing, *Science* **346**, 328 (2014).

[13] H. Hodaei, A. U. Hassan, S. Wittek, H. Garcia-Gracia, R. El-Ganainy, D. N. Christodoulides, and M. Khajavikhan, Enhanced sensitivity at higher-order exceptional points, *Nature* **548**, 187 (2017).

[14] H. Xu, D. Mason, L. Jiang, and J. G. E. Harris, Topological energy transfer in an optomechanical system with exceptional points, *Nature* **537**, 80 (2016).

[15] D. Zhang, X.-Q. Luo, Y.-P. Wang, T.-F. Li, and J. Q. You, Observation of the exceptional point in cavity magnon-polaritons, *Nature Communications* **8**, 1368 (2017).

[16] M. Partanen, J. Goetz, K. Y. Tan, K. Kohvakka, V. Sevriuk, R. E. Lake, R. Kokkonieni, J. Ikonen, D. Hazra, A. Makinen, E. Hyypa, L. Gronberg,

V. Vesterinen, M. Silveri, and M. Mottonen, Exceptional points in tunable superconducting resonators, *Phys. Rev. B* **100**, 134505 (2019).

[17] C. Shi, M. Dubois, Y. Chen, L. Cheng, H. Ramezani, Y. Wang, and X. Zhang, Accessing the exceptional points of parity-time symmetric acoustics, *Nature Communications* **7**, 11110 (2016).

[18] W. Chen, S. K. Ozdemir, G. Zhao, J. Wiersig, and L. Yang, Exceptional points enhance sensing in an optical microcavity, *Nature* **548**, 192 (2017).

[19] H.-K. Lau and A. A. Clerk, Fundamental limits and non-reciprocal approaches in non-hermitian quantum sensing, *Nature Communications* **9**, 4320 (2018).

[20] M. Naghiloo, M. Abbasi, Y. N. Joglekar, and K. W. Murch, Quantum state tomography across the exceptional point in a single dissipative qubit, *Nature Physics* **15**, 1232 (2019).

[21] W. Chen, M. Abbasi, Y. N. Joglekar, and K. W. Murch, Quantum jumps in the non-hermitian dynamics of a superconducting qubit, *Phys. Rev. Lett.* **127**, 140504 (2021).

[22] F. Minganti, A. Miranowicz, R. W. Chhajlany, and F. Nori, Quantum exceptional points of non-hermitian hamiltonians and liouvillians: The effects of quantum jumps, *Phys. Rev. A* **100**, 062131 (2019).

[23] A. Blais, A. L. Grimsmo, S. M. Girvin, and A. Wallraff, Circuit quantum electrodynamics, *Rev. Mod. Phys.* **93**, 025005 (2021).

[24] J. Koch, T. M. Yu, J. Gambetta, A. A. Houck, D. I. Schuster, J. Majer, A. Blais, M. H. Devoret, S. M. Girvin, and R. J. Schoelkopf, Charge-insensitive qubit design derived from the cooper pair box, *Phys. Rev. A* **76**, 042319 (2007).

[25] P. Lewalle, S. K. Manikandan, C. Elouard, and A. N. Jordan, Measuring fluorescence to track a quantum emitter's state: a theory review, *Contemporary Physics*, *Contemporary Physics* **61**, 26 (2020).

[26] A. N. Jordan, A. Chantasri, P. Rouchon, and B. Huard, Anatomy of fluorescence: quantum trajectory statistics from continuously measuring spontaneous emission, *Quantum Studies: Mathematics and Foundations* **3**, 237 (2016).

[27] M. Naghiloo, D. Tan, P. M. Harrington, P. Lewalle, A. N. Jordan, and K. W. Murch, Quantum caustics in resonance-fluorescence trajectories, *Phys. Rev. A* **96**, 053807 (2017).

[28] P. Campagne-Ibarcq, P. Six, L. Bretheau, A. Sarlette, M. Mirrahimi, P. Rouchon, and B. Huard, Observing quantum state diffusion by heterodyne detection of fluorescence, *Phys. Rev. X* **6**, 011002 (2016).

[29] M. Naghiloo, N. Foroozani, D. Tan, A. Jadbabaie, and K. W. Murch, Mapping quantum state dynamics in spontaneous emission, *Nature Communications* **7**, 11527 (2016).

[30] D. Tan, N. Foroozani, M. Naghiloo, A. H. Kiilerich, K. Molmer, and K. W. Murch, Homodyne monitoring of postselected decay, *Phys. Rev. A* **96**, 022104 (2017).

[31] Q. Ficheux, S. Jezouin, Z. Leghtas, and B. Huard, Dynamics of a qubit while simultaneously monitoring its relaxation and dephasing, *Nature Communications* **9**, 1926 (2018).

[32] H. M. Wiseman, Quantum trajectories and quantum measurement theory, *Quantum and Semiclassical Optics*: *Journal of the European Optical Society Part B* **8**, 205 (1996).

[33] D. Steck, *Quantum and Atom Optics* (2007).

[34] H. M. Wiseman and G. J. Milburn, *Quantum Measurement and Control* (Cambridge University Press, Cambridge, 2009).

[35] H. M. Wiseman and G. J. Milburn, Quantum theory of optical feedback via homodyne detection, *Phys. Rev. Lett.* **70**, 548 (1993).

[36] S. J. Weber, A. Chantasri, J. Dressel, A. N. Jordan, K. W. Murch, and I. Siddiqi, Mapping the optimal route between two quantum states, *Nature* **511**, 570 (2014).

[37] A. N. Jordan, Watching the wavefunction collapse, *Nature* **502**, 177 (2013).

[38] K. Mølmer, Y. Castin, and J. Dalibard, Monte carlo wave-function method in quantum optics, *Journal of the Optical Society of America B*, *J. Opt. Soc. Am. B* **10**, 524 (1993).

[39] A. Bolund and K. Mølmer, Stochastic excitation during the decay of a two-level emitter subject to homodyne and heterodyne detection, *Phys. Rev. A* **89**, 023827 (2014).

[40] K. Jacobs and D. A. Steck, A straightforward introduction to continuous quantum measurement, *Contemporary Physics*, *Contemporary Physics* **47**, 279 (2006).

[41] A. N. Korotkov, Quantum bayesian approach to circuit qed measurement with moderate bandwidth, *Phys. Rev. A* **94**, 042326 (2016).

[42] K. W. Murch, S. J. Weber, C. Macklin, and I. Siddiqi, Observing single quantum trajectories of a superconducting quantum bit, *Nature* **502**, 211 (2013).

[43] Z. K. Minev, S. O. Mundhada, S. Shankar, P. Reinhold, R. Gutiérrez-Jáuregui, R. J. Schoelkopf, M. Mirrahimi, H. J. Carmichael, and M. H. Devoret, To catch and reverse a quantum jump mid-flight, *Nature* **570**, 200 (2019).

[44] J. Gambetta, A. Blais, M. Boissonneault, A. A. Houck, D. I. Schuster, and S. M. Girvin, Quantum trajectory approach to circuit qed: Quantum jumps and the zeno effect, *Phys. Rev. A* **77**, 012112 (2008).

[45] N. Gisin, Quantum measurements and stochastic processes, *Phys. Rev. Lett.* **52**, 1657 (1984).

[46] A. Barchielli, Measurement theory and stochastic differential equations in quantum mechanics, *Phys. Rev. A* **34**, 1642 (1986).

[47] A. Chantasri, J. Dressel, and A. N. Jordan, Action principle for continuous quantum measurement, *Phys. Rev. A* **88**, 042110 (2013).

[48] A. Chantasri and A. N. Jordan, Stochastic path-integral formalism for continuous quantum measurement, *Phys. Rev. A* **92**, 032125 (2015).

[49] P. Lewalle, A. Chantasri, and A. N. Jordan, Prediction and characterization of multiple extremal paths in continuously monitored qubits, *Phys. Rev. A* **95**, 042126 (2017).

[50] T. Karmakar, P. Lewalle, and A. N. Jordan, Stochastic path-integral analysis of the continuously monitored quantum harmonic oscillator, *PRX Quantum* **3**, 010327 (2022).

[51] P. Lewalle, J. Steinmetz, and A. N. Jordan, Chaos in continuously monitored quantum systems: An optimal-path approach, *Phys. Rev. A* **98**, 012141 (2018).

[52] P. Lewalle, Quantum trajectories and their extremal-probability paths: New phenomena and applications, Thesis.